RSC Advances

PAPER

View Article Online
View Journal | View Issue



Cite this: *RSC Adv.*, 2022, **12**, 30605

# Regulating the pyrolysis process of cation intercalated $MnO_2$ nanomaterials for electrocatalytic urea oxidation performance†

Yuxin Shi,[a] Jianing Li,[a] Xu Zhang,[a] Kai Zhao,[a] Zheng Wang,*[a] Zhao Wang*[b] and Xu Peng *[a]

Received 30th June 2022
Accepted 20th October 2022

DOI: 10.1039/d2ra04032h

rsc.li/rsc-advances

Exploring an efficient way to enhance electron/ion transport behavior of nanomaterials plays an important role in the study of energy storage & conversion. However, the evolution rules of lattice and electronic structure during the pyrolysis process of low-dimensional nanomaterials, which further regulate its electron/ion transport properties, have not been effectively elucidated. Here we study the pyrolysis process of cation intercalated $MnO_2$ as a case for realizing optimized electron/ion transport behavior. In our case, thermogravimetry-mass spectrometry (TG-MS) was adopted for tracking the remaining products in pyrolysis and decomposition products, further finding out the evolution law of the manganese–oxygen polyhedron structure during the pyrolysis. Moreover, the internal relations between the crystal structure and the electronic structure during the pyrolysis process of low-dimensional manganese oxide are revealed by fine structure characterization. As expected, partially treated 2D $MnO_2$ nanosheets with controlled pyrolysis displays ultrahigh UOR performance with the overpotential of 1.320 V *vs.* RHE at the current density of 10 mA $cm^{-2}$, which is the best value among non-nickel-based materials. We anticipate that studying the mechanism of the pyrolysis process has important guiding significance for the development of high electron/ion transport devices.

## Introduction

The most efficient way to convert and store energy is to achieve the mutual conversion between electrical energy and chemical energy.[1–3] As a carrier for energy conversion and storage, electron/ion transport properties determine the expression of functional behavior.[4] Therefore, finding efficient material systems and effective research methods is the key to improving the performance of electron/ion transport. So far, the mainstream systems for studying electron/ion transport performance materials are perovskite materials,[5] inorganic 3d transition metal oxides/chalcogenides/nitrides,[6–8] metal organic frameworks (MOF), *etc.*[9–15] These material systems have made great progress in the study of electron/ion transport properties, providing us with extensive experience in optimizing the structure of electron/ion transport properties through the development and in-depth study of one of the material systems. Of note, manganese oxide provides a good material platform for the regulation of novel electronic states due to its easy regulation property.[16] Manganese oxide is usually composed of manganese oxygen polyhedron, while different Mn valence and manganese oxygen coordination form determines its special physicochemical behavior.[17–25] For example, the trivalent manganese ion may have the Jahn–Teller effect, causing Jahn–Teller distortion in the system, resulting in a special electronic structure.[26] Besides, when trivalent manganese ions and tetravalent manganese ions coexist in the $MnO_6$ octahedron system, double exchange effect may be generated, resulting in novel magnetic and electrical transport properties.[27,28] Moreover, when divalent manganese ions are arranged in a face-centered cubic manner in MnO, super-exchange structure would be produced, which can be used to explain the phenomenon of anti-ferromagnetic spontaneous magnetization.[29] Therefore, regulating the valence state of manganese ion and manganese oxygen coordination form of manganese oxide provides an ideal model for studying the electronic structure of the material and finding out the influencing factors that affect the electron/ion transport performance. As an effective route of in-depth analysis of materials, pyrolysis has made considerable progress in recent years, especially qualitative research on as-pyrolysis products. In general, pyrolysis of materials is carried out by controlled temperature heating in a furnace or CVD/PVD/ALD

[a]Hubei Collaborative Innovation Center for Advanced Organic Chemical Materials, Ministry-of-Education Key Laboratory for the Synthesis and Application of Organic Functional Molecules & College of Chemistry & Chemical Engineering, Hubei University, Wuhan, 430062, P. R. China. E-mail: pengxu@hubu.edu.cn; zwang@hubu.edu.cn

[b]Equine Science Research and Horse Doping Control Laboratory Wuhan Business University, Wuhan 430056, People's Republic of China. E-mail: wangzhao517@stu.hubu.edu.cn

† Electronic supplementary information (ESI) available. See DOI: https://doi.org/10.1039/d2ra04032h

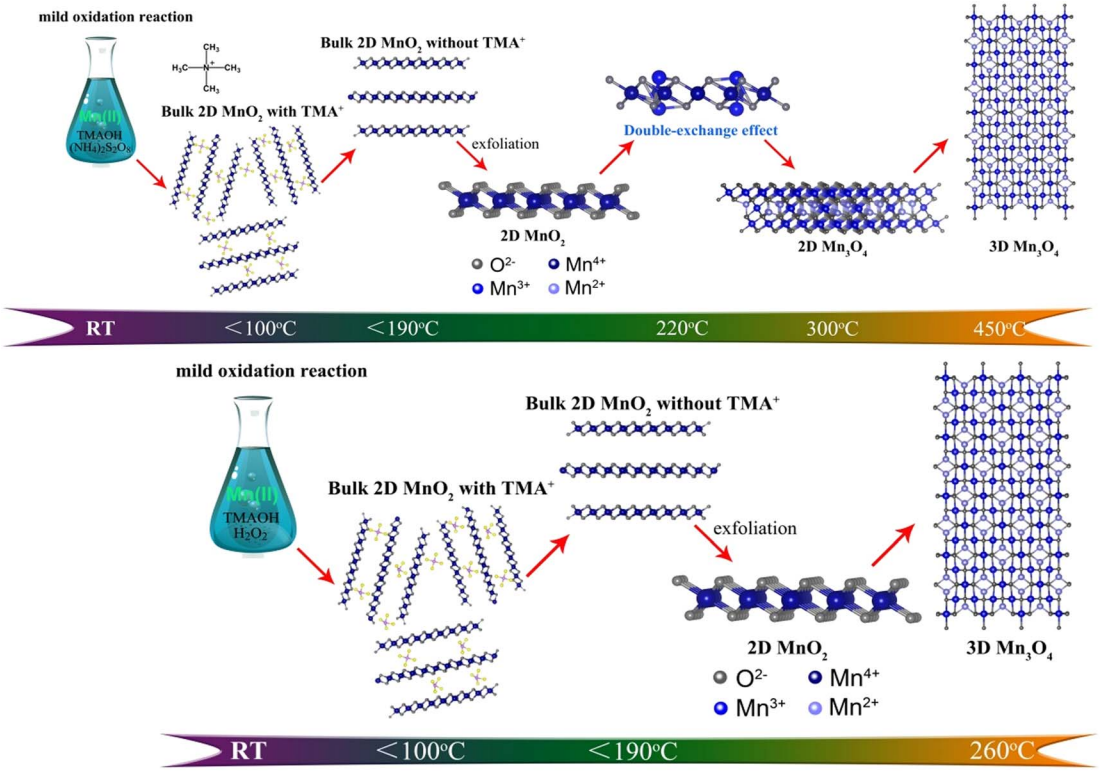


Scheme 1 The schematic illusion of evolution process of two different types of 2D $MnO_2$ nanomaterials during pyrolysis process.

method.[30] However, pyrolysis is generally viewed as a means to obtain the target product through high-temperature chemical reactions, without a thorough understanding of materials in the pyrolysis process. In order to analyze the pyrolysis process, the method of TG analysis is usually used to analyze the quality variation of the material during the pyrolysis process, which combined with the differential scanning calorimetry (DSC) to monitor thermodynamic process that takes place on pyrolysis. Moreover, the development of TG-MS coupled with mass spectrometry (MS) provides abundant information for further studying the pyrolysis process. Currently, TG-MS is mostly used to analyze well-defined materials such as graphene,[31] carbon nanotubes,[32] iron oxide[33] and so on. TG-MS combines TG and MS to detect very low levels of impurities. During the pyrolysis of the sample, the sample thermally decomposes and volatilizes out of the gas, which is transmitted to the mass spectrometer for identification.[34] Therefore, TG-MS can be used to pyrolyze materials with well-defined structure, and the pyrolysis residual products and decomposition products can be regulated by different pyrolysis temperature and holding time to further study the pyrolysis reaction process of materials to obtain functional materials with different electronic structures. Here we take advantage of TG-MS tracking of pyrolysis processes in real-time. In our case, the evolution low of their lattice and electronic structure of cation intercalated 2D $MnO_2$ nanomaterials were successfully elucidated, further successfully realizing the controllable synthesis of low-dimensional $MnO_x$ with controlled specific surface area, more active sites, significant improved conductivity. As expected, 2D-$MnO_2$-550 nanosheet with controlled pyrolysis displays ultrahigh UOR performance with the overpotential of 1.320 V *vs.* RHE at the current density of 10 mA $cm^{-2}$ (Scheme 1).

## Results and discussions

In order to further clarify the pyrolysis process and mechanism of $MnO_2$, we chose three typical low-dimensional manganese dioxides as reference: Two kinds of 2D birnessite $MnO_2$, colloidal birnessite $MnO_2$ (H-$MnO_2$) and bulk $MnO_2$ (1D-$MnO_2$), as we previously reported. And one-dimensional $MnO_2$ nanowire as reported in literature (Fig. 1). Notably, the 1D $MnO_2$ nanowire has no cation intercalated behavior, which can be seen as typical $MnO_2$. While two kinds of 2D birnessite $MnO_2$

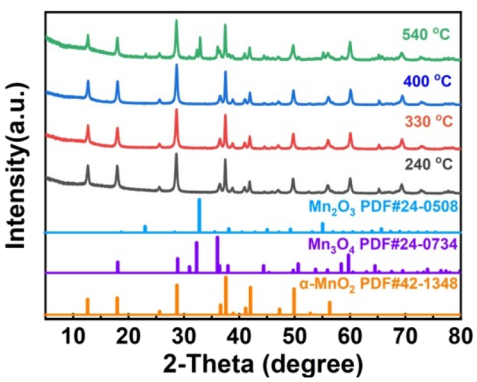


Fig. 1 PXRD pattern of 1D-$MnO_2$ at different pyrolysis temperatures.

both have $TMA^+$ intercalated in the layers of 2D $MnO_2$. The difference between these two kinds of 2D birnessite $MnO_2$ is the physical characteristics of materials, of which one is colloidal and other is powder-like. As shown in Fig. 2a, the pyrolysis process is first studied *via* TG analysis underwent helium atmosphere. As expected, the 1D $MnO_2$ nanowire with no cation intercalated has typical $MnO_2$ decomposition behavior in TG curves. The remaining weight percentage is 90%, which can be assigned to the transformation to $Mn_3O_4$ (Fig. S1†), where the pyrolysis in a low oxygen partial pressure environment can lead to the escape of O elements. In contrast, the two kinds of the cation intercalated 2D $MnO_2$ with tetramethylammonium hydroxide ($TMA^+$) ions more distinct TG curves. For H-$MnO_2$, there is significant weight loss around 200 °C, and the weight loss rate is 11%. The remaining weight percentage is 72%. Meanwhile, for 2D-$MnO_2$, have obvious transition characteristics in thermogravimetric analysis. The weight loss area is more rich than other materials, there are three weight loss parts, and the remaining weight percentage is 70%.

We first analyzed the two-dimensional $MnO_2$ nanomaterials with different pyrolysis temperatures by X-ray diffraction (XRD) (Fig. 2b). It should be noted that when the pyrolysis temperature of 2D-$MnO_2$ is higher than 400 °C, only $Mn_3O_4$ can be observed in the resulting material (JCPDS No. 24-0734). The diffraction peaks at 17.7°, 28.7°, 32.1°, 35.8°, 44.2°, 59.6° and 64.4° can assign to (101), (112), (103), (211), (220), (224) and (400) lattice plane. clearly shows that 2D-$MnO_2$ nanomaterials still maintain two-dimensional morphology at 500 °C, and are nanoflowers formed by the aggregation of nanosheets (Fig. S2†). Under the condition of small temperature range, the phase of H-$MnO_2$ has changed greatly, which leads to further exploration of the compounds (Fig. S3†). In this paper, we hope to study the fine electronic states of H-$MnO_2$-190, -220, -260, especially in the Mn state, to observe the changes in pyrolysis. We have carried out Mn $L_3$ side XAS tests on compounds H-$MnO_2$-190, -220, -260 (Fig. 2d). It can be seen from the spectrum that the edge of Mn $L_3$ is divided into two parts because the Mn 3d orbital of Oh symmetry is divided into two groups: $e_g$ and $t_{2g}$. The edge spectra of Mn $L_3$ show that the intensity of the transition peak increases at $2p \rightarrow t_{2g}$, and the valence states of H-$MnO_2$-260, -220 increase. This fact shows that compared with compound H-$MnO_2$-190, the 3d orbital of Mn in compounds H-$MnO_2$-260 and H-$MnO_2$-220 with higher pyrolysis temperature has the phenomenon of electron transfer, and the electron injection process occurs.[35] At the same time, the lower valence state is also reflected in the absorption shift of Mn $L_3$ edge. Compared with compound H-$MnO_2$-190, the absorption edge of compound H-$MnO_2$-260, -220 shifts in the low energy direction.

In order to analyze the structure of low-dimensional $MnO_2$ nanomaterials during pyrolysis, thermogravimetric analysis and mass spectrometry (TG-MS) were used. With a constant flow rate of helium gas of 5 mL $min^{-1}$, the sample was heated from room temperature (RT) to 800 °C, and then the thermally separated entities were analyzed by an EI mass spectrometer. As shown in Fig. 3, the three main steps of mass loss detection are Area A: 100 to 310 °C, Area B: 470–580 °C and Area C: 620–780 °C. The first step (Area A) starts with showing only the molecular fragments of *m*/*z* 16 and 18, because the residues of water and $TMA^+$ have been inserted between the δ-$MnO_2$ nanosheet layers. It was found that the structure of δ-$MnO_2$ nanosheets was consistent, and $TMA^+$ molecules began to decompose at 140 °C. At around 270 °C, *m*/*z* 16, 18 and 44 show a series of different peaks. These facts indicate that δ-$MnO_2$ nanosheets are converted into $Mn_3O_4$ nanosheets together with oxygen atoms from octahedral $MnO_6$ structure from δ-$MnO_2$ octahedral $MnO_6$ structure to $Mn_3O_4$ tetrahedral $MnO_4$ structure. In the second step (region B), only *m*/*z* 64 molecular fragments were detected, indicating that the $(CH_3)_3N$ molecules generated by $TMA^+$ molecular pyrolysis had been intercalated with δ-$MnO_2$ nanosheets before 470 °C, and maintained a two-dimensional structure. In the third step (region C), the molecular fragments of *m*/*z* 64 and *m*/*z* 32 were detected (Fig. S4†). At this time, $MnO_2$ had been completely transformed into $Mn_3O_4$ nanosheets, and with the loss of intercalated $(CH_3)_3N$ molecules, the two-dimensional structure collapsed. The possible reactions include:

$$3MnO_2 \rightarrow Mn_3O_4 + O_2 \quad (1)$$

$$(CH_3)_4N^+ + OH^- \rightarrow CH_4 + (CH_3)_3N + \tfrac{1}{2}O_2 \quad (2)$$

$$CH_4 + 2O_2 \rightarrow CO_2 + 2H_2O \quad (3)$$

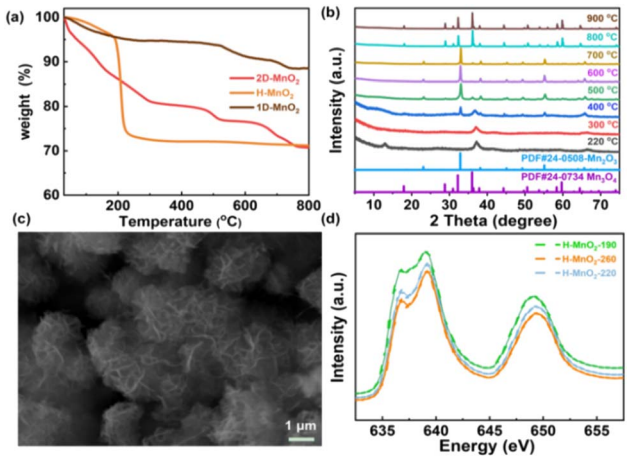


Fig. 2 (a) TG curves of three types of $MnO_2$, (b) XRD patterns of 2D-$MnO_2$ at 220–1000 °C, (c) SEM images of 2D-$MnO_2$ at 550 °C, (d) Mn $L_3$ edge XAS of H-$MnO_2$, -190, -220, -260.

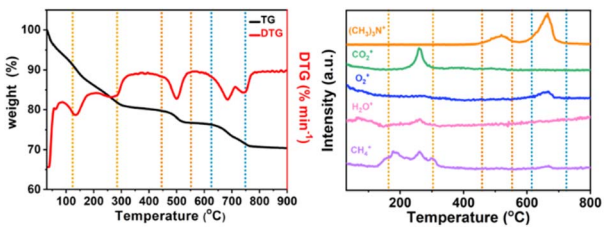


Fig. 3 TG-MS analysis of low-dimensional $MnO_2$ nano-materials. TG curves of (a) 2D-$MnO_2$, (b) MS trace of 2D-$MnO_2$ at RT ~ 800 °C.

As shown in Fig. 3a, H-$MnO_2$ only has a significant weightless area, ie 200 °C to 300 °C, while MS only detected a significant peak range in this area (Fig. S5†). These peaks can be explained by the decomposition of $TMA^+$ molecules and the conversion of δ-$MnO_2$ to $Mn_3O_4$. The structural evolution of $MnO_2$ nanosheets during pyrolysis was also confirmed by XRD patterns of $MnO_2$ nanosheets at different pyrolysis temperatures. The change of phase during pyrolysis was explored by XRD (Fig. 2). The diffraction peaks of 240 °C and 400 °C α-$MnO_2$ are still clear and sharp on its pyrolysis process (Fig. S5†). When the temperature rises to 400 °C, two new diffraction peaks appear. The diffraction peaks at 32.3° are in line with the (103) crystal surface of $Mn_3O_4$ (JCPDS Card No. 24-0734), and the diffraction peaks at 32.9° match with (222) crystal surface of $Mn_2O_3$ (JCPDS Card No. 24-0508). This indicates that the phase changes at 400 °C, and it is likely to contain three manganese oxides. In order to further understand the pyrolysis process of different $MnO_2$, one-dimensional manganese dioxide was also analyzed by TG-MS (Fig. 4). From the TG curve, it can be seen that the compound is stable δ-$MnO_2$ the mass percent loss of $MnO_2$ is not much. At 800 °C, the total loss is 10%. The trend of the curve is similar to that of typical $MnO_2$, indicating that there is no intercalation structure. No other special molecular fragments were found in MS. After 500 °C, there are two slight weightlessness, with a weight loss of 6%. This part also shows the change of biological phase in XRD analysis. This weightlessness may due to the loss of oxygen in the lattice of manganese oxide, resulting in the change of valence state.[36] To further explore the structural changes of $MnO_2$/NF composites, we conducted X-ray photoelectron spectroscopy (XPS) to effectively study the chemical composition, as shown in Fig. S7–S8.†

We used a typical three-electrode configuration in 1 M KOH electrolyte and 0.33 M urea to perform electrochemical tests on three different $MnO_2$ pyrolyzed at different temperatures. The loading of the catalyst on the nickel foam was 1.68 mg $cm^{-2}$. As shown in Fig. 6a and Fig. S9–S11† in a typical linear sweep voltammogram (LSV) plot, the anodic current of all samples simultaneously increases as the potential becomes more positive. The 2D-$MnO_2$-550 electrode displayed the smaller overpotential of 1.320 V (at the current density of 10 mA $cm^{-2}$) than other samples such as H-$MnO_2$-260 (1.383 V), 1D-$MnO_2$-400 (1.393 V) and nickel foam (1.391 V). The UOR kinetics of the catalyst was studied by the corresponding Tafel diagram. As shown in Fig. 6b, the Tafel slope of 2D-$MnO_2$-550 is calculated to be 21.5 mV $dec^{-1}$. It is lower than the Tafel slope of H-$MnO_2$-260 (25 mV $dec^{-1}$). This also proves that two-dimensional materials are better than one-dimensional materials in UOR. This also proves the advantages of two-dimensional $MnO_2$ over one-dimensional $MnO_2$ in terms of UOR. In order to further prove that 2D-$MnO_2$-550 has the most efficient electrocatalytic urea oxidation performance, we evaluated the electrochemical double-layer capacitance ($C_{dl}$) and electrochemical surface area (ECSA) indexes of 2D-$MnO_2$-550, H-$MnO_2$-260 and 1D-$MnO_2$-400 by cyclic voltammetry (Fig. 5).[37–39] Fig. 5 shows the linear fitting curve of $\Delta j$ with different scanning rates (6, 8, 10, 12, 14 and 16 mV $s^{-1}$). The ECSA of 2D-$MnO_2$-550 sample has a maximum value of 19.22 mF $cm^{-2}$. The ECSA of other samples 1D-$MnO_2$-400 was 11.95 mF $cm^{-2}$ and that of H-$MnO_2$-260 was 4.66 mF $cm^{-2}$ (Fig. 5d). Therefore, this shows that 2D-$MnO_2$-550

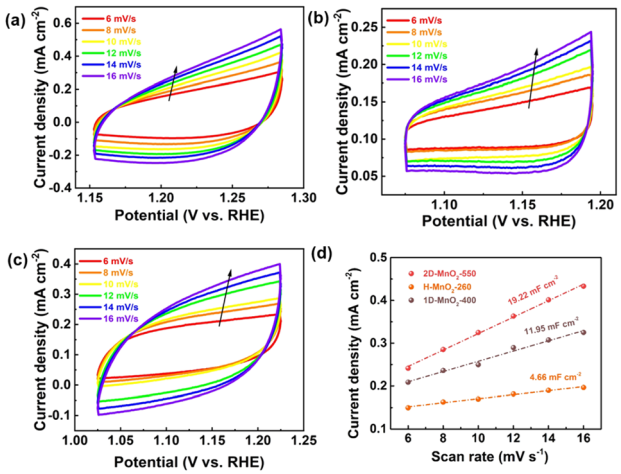


Fig. 5 (a) CVs of 2D-$MnO_2$-550. (b) CVs of H-$MnO_2$-260. (c) CVs of 1D-$MnO_2$-400. (d) Electrocatalytic specific surface area of 2D-$MnO_2$-550, H-$MnO_2$-260 and 1D-$MnO_2$-400.

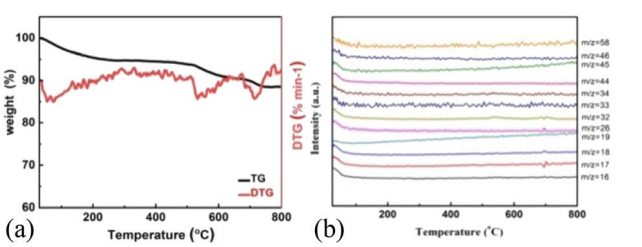


Fig. 4 TG-MS analysis of low-dimensional $MnO_2$ nano-materials. TG curves of (a) 1D-$MnO_2$, (b) MS trace of 1D-$MnO_2$ at RT ~ 800 °C.

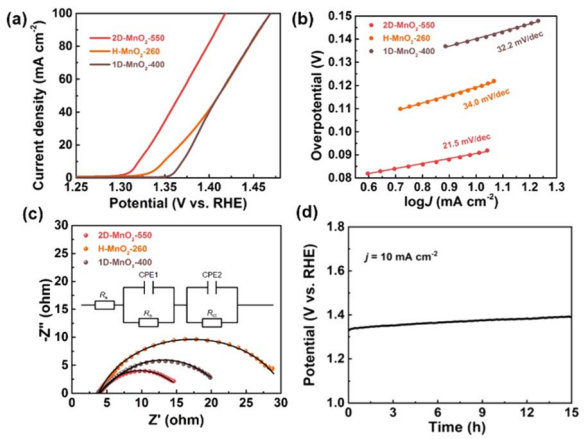


Fig. 6 UOR performance of three types of $MnO_2$. (a) LSV plots of 2D-$MnO_2$-550, H-$MnO_2$-260 and 1D-$MnO_2$-400. (b) Tafel plots of 2D-$MnO_2$-550, H-$MnO_2$-260 and 1D-$MnO_2$-400. (c) Electrochemical impedance spectroscopy (EIS) of 2D-$MnO_2$-550, H-$MnO_2$-260 and 1D-$MnO_2$-400. (d) Long-term durability measured at a constant current density of 10 mA $cm^{-2}$ for 15 h in 1 M KOH + 0.33 M Urea solution, respectively.

materials can provide more exposed electrocatalytic active sites and have more catalytic activity in the electrolysis process.[40]

At the same time, the UOR kinetics of the prepared electrode was further evaluated by electrochemical impedance spectroscopy (EIS). The semicircle of H-$MnO_2$-260 sample is the largest, and the charge transfer resistance is also the largest, which may be related to the state of the sample. Because H-$MnO_2$ is colloidal and difficult to disperse, the resistance is too large. We use zview software to fit the measured AC impedance, and the black line is the fitting result (Fig. 6c). According to the fitting results, the pattern of the equivalent circuit diagram is $R_s$ (CPE1, $R_o$) (CPE2, $R_{ct}$),[41] in which the charge transfer resistance ($R_{ct}$) at the catalyst/electrolyte interface of sample 2D-$MnO_2$-550 is the smallest, with a value of 7.69 Ω. The $R_{ct}$ of samples H-$MnO_2$-260 and 1D-$MnO_2$-400 are 18.44 Ω and 8.08 Ω, respectively. The solution resistance ($R_s$) of the three samples is about 3.8 Ω. CPE1 and CPE2 describe the electron transport at the electrode material/catalyst interface and catalyst/electrolyte interface respectively, and $R_o$ represents the oxide film resistance at the catalyst/electrolyte interface.[42] Because 3D macroporous nickel foam has been widely used as an electrocatalyst carrier, we have tested the stability of the sample 2D-$MnO_2$-550 loaded with nickel foam in 1 M KOH and 0.33 M urea solutions. In this experiment, the chronopotentiometry was used to test under the current density of 10 mA $cm^{-2}$. As shown in Fig. 6d, sample 2D-$MnO_2$-550 lasted for 15 hours at a current density of 10 mA $cm^{-2}$, with a voltage increase of 4.5%, indicating that the sample can stably carry out a long-term catalytic reaction.[43]

## Conclusions

In summary, we have shown how to the cation intercalated 2D $MnO_2$ featuring $TMA^+$ cation underwent TG-MS controlled pyrolysis can be realized as promoted electrocatalytic urea oxidation performance with distinct $MnO_x$ nanostructures. We directly confirm the evolution law of residual of cation intercalated $MnO_2$ nanomaterials, which is responsible for the evolution law of composition of cation intercalated $MnO_2$ nanomaterials by TG-MS, and thus clarifying the high-performance with distinct $MnO_x$ structure. As expected, partially treated 2D $MnO_2$ nanosheet with controlled pyrolysis displays ultrahigh UOR performance with the overpotential of 1.320 V *vs.* RHE at the current density of 10 mA $cm^{-2}$. This novel strategy of controlled pyrolysis by TG-MS offering a potential to become a bifunctional energy nanodevice with high electron/ion transport behavior.

## Conflicts of interest

There are no conflicts to declare.

## Acknowledgements

This work was financially supported by the National Science Fund for NSFC (Grants 21805074), and NSFC of Hubei (Grants 2021CFB420).

## Notes and references

1 P. Simon, Y. Gogotsi and B. Dunn, *Science*, 2014, **343**, 1210.
2 P. Simon and Y. Gogotsi, *Nat. Mater.*, 2008, **7**, 845.
3 X. Peng, L. Peng, C. Wu and Y. Xie, *Chem. Soc. Rev.*, 2014, **43**, 3303.
4 H. A. Gasteiger and N. M. Marković, *Science*, 2009, **324**, 48.
5 E. Dagotto, *Science*, 2005, **309**, 257.
6 L. Peng, P. Xiong, L. Ma, Y. Yuan, Y. Zhu, D. Chen, X. Luo, J. Lu, K. Amine and G. Yu, *Nat. Commun.*, 2017, **8**, 15139.
7 M. Chhowalla, H. S. Shin and G. Eda, *Nat. Chem.*, 2013, **5**, 263.
8 Y. Zhang, B. Ouyang and J. Xu, *Angew. Chem., Int. Ed.*, 2016, **55**, 8670–8674.
9 X. Lu, P. Liao and J. Wang, *J. Am. Chem. Soc.*, 2016, **138**, 8336–8339.
10 J. Q. Zhao, D. D. Cai, J. Dai, M. Kurmoo, X. Peng and M. H. Zeng, *Sci. Bull.*, 2019, **64**, 1667–1674.
11 B. X. Pan, X. Peng, Y. F. Wang, Q. An, X. Zhang, Y. X. Zhang, T. S. Teets and M. H. Zeng, *Chem. Sci.*, 2019, **10**, 4560–4566.
12 Y. Wang, Y. Liang, Y. Wu, J. Yang, X. Zhang, D. Cai, X. Peng and M. H. Zeng, *Angew. Chem., Int. Ed.*, 2020, **59**, 13232–13237.
13 Q. An, B. X. Pan, L. Li, X. Peng and M. H. Zeng, *Chin. J. Chem.*, 2021, **39**, 2529–2535.
14 X. Zhang, K. Zhao, X. Peng, M. Kurmoo and M. H. Zeng, *Nano Res.*, 2022, **15**, 346–351.
15 L. Li, L. Wang, S. Tao, X. Peng and M. H. Zeng, *Inorg. Chem. Front.*, 2022, **9**, 1973–1983.
16 F. Qi, K. Hirofumi and O. Kenta, *J. Mater. Chem.*, 1999, **9**, 319–333.
17 Y. Hu, Y. Wu and J. Wang, *Adv. Mater.*, 2018, **30**, 1802569.
18 S. V. Streltsov and D. I. Khomskii, *Phys. Rev. X*, 2020, **10**, 031043.
19 L. S. Suib, *J. Mater. Chem.*, 2008, **18**, 1623–1631.
20 F. Cheng, Y. Su, J. Liang, Z. Tao and J. Chen, *Chem. Mater.*, 2010, **22**, 898–905.
21 M. Toupin, T. Brousse and D. Bélanger, *Chem. Mater.*, 2004, **16**, 3184–3190.
22 S. Devaraj and N. Munichandraiah, *J. Phys. Chem. C*, 2008, **112**, 4406–4417.
23 A. Bergmann, I. Zaharieva, H. Dau and P. Strasser, *Energy Environ. Sci.*, 2013, **6**, 2745–2755.
24 K. L. Pickrahn, S. W. Park and Y. Gorlin, *Adv. Energy Mater.*, 2012, **2**(10), 1269–1277.
25 A. Ramírez, P. Hillebrand and D. Stellmach, *J. Phys. Chem. C*, 2014, **118**, 14073–14081.
26 S. V. Streltsov and D. I. Khomskii, *Phys. Rev. X*, 2020, **10**, 031043.
27 X. Peng, Y. Guo and Q. Yin, *J. Am. Chem. Soc.*, 2017, **139**, 5242–5248.
28 S. Jin, T. H. Tiefel, M. McCormack, R. A. Fastnacht, R. Ramesh and L. H. Chen, *Science*, 1994, **264**, 413.
29 Y. Zhou, S. Sun and S. Xi, *Adv. Mater.*, 2017, 1700874.
30 T. J. Kempa, E. C. Sadler and T. Chowdhury, *Chem. Rev.*, 2020, **120**(22), 12563–12591.

31 Z. Sebestyén, E. Barta-Rajnai and Z. Czégény, *Energy Fuels*, 2016, **30**(10), 7982–7993.
32 F. Hof, S. Bosch and S. Eigler, *J. Am. Chem. Soc.*, 2013, **135**, 18385–18395.
33 S. G. Kwon, Y. Piao and J. Park, *J. Am. Chem. Soc.*, 2007, **129**, 12571.
34 R. Schäfer, D. Dasler and U. Mundloch, *J. Am. Chem. Soc.*, 2016, **138**, 1647–1652.
35 J. C. Wu, X. Peng and Y. Q. Guo, *Front. Phys.*, 2018, **13**(3), 138110.
36 X. Zhang, W. Yang and J. Yang, *J. Cryst. Growth*, 2008, **310**, 716–722.
37 Q. Liu, L. Xie and F. Qu, *Inorg. Chem. Front.*, 2017, **4**, 1120.
38 C. Wei, S. N. Sun and X. Wang, *Chem. Soc. Rev.*, 2019, **48**, 2518–2534.
39 G. F. Li, Y. N. Chen and M. Pan, *Sustainable Energy Fuels*, 2018, **2**, 237–251.
40 Y. Tong, P. Chen and M. Zhang, *ACS Catal.*, 2018, **8**(1), 1–7.
41 L. Wang, L. Ren and X. Wang, *ACS Appl. Mater. Interfaces*, 2018, **10**, 4750–4756.
42 J. Zhang, F. Li and W. Chen, *Electrochim. Acta*, 2019, **300**, 123–130.
43 D. Zhu, C. Guo and J. Liu, *Chem. Commun.*, 2017, **53**, 10906–10909.